

# Numerical analysis of contact line dynamics passing over a single wettable defect on a wall

Cite as: Phys. Fluids **28**, 082109 (2016); <https://doi.org/10.1063/1.4961490>

Submitted: 20 February 2016 . Accepted: 10 August 2016 . Published Online: 31 August 2016

Yasufumi Yamamoto , Shohei Higashida, Hiroyuki Tanaka, Tatsuro Wakimoto, Takahiro Ito, and Kenji Katoh



[View Online](#)



[Export Citation](#)



[CrossMark](#)

## ARTICLES YOU MAY BE INTERESTED IN

### Contact line dynamics on heterogeneous surfaces

Physics of Fluids **23**, 072103 (2011); <https://doi.org/10.1063/1.3609817>

### Boundary conditions for the moving contact line problem

Physics of Fluids **19**, 022101 (2007); <https://doi.org/10.1063/1.2646754>

### Continuum models for the contact line problem

Physics of Fluids **22**, 102103 (2010); <https://doi.org/10.1063/1.3501317>



CAPTURE WHAT'S POSSIBLE  
WITH OUR NEW PUBLISHING ACADEMY RESOURCES

[Learn more](#) 

# Numerical analysis of contact line dynamics passing over a single wettable defect on a wall

Yasufumi Yamamoto,<sup>1,a)</sup> Shohei Higashida,<sup>2</sup> Hiroyuki Tanaka,<sup>2</sup>  
Tatsuro Wakimoto,<sup>2</sup> Takahiro Ito,<sup>3</sup> and Kenji Katoh<sup>2</sup>

<sup>1</sup>Department of Mechanical Engineering, Kansai University, 3-35, Yamate-cho 3-chome, Saitama, Japan 356-8680, Japan

<sup>2</sup>Department of Mechanical Engineering, Osaka City University, 3-3-138, Sumiyoshi-ku Sugimoto, Osaka 558-8585, Japan

<sup>3</sup>Department of Energy Engineering and Science, Nagoya University, Chikusa-ku Furo-cho, Nagoya 464-8603, Japan

(Received 20 February 2016; accepted 10 August 2016; published online 31 August 2016)

In this study, the dynamics of a contact line passing a single defect, which was represented by a locally wettable part (whose static contact angle is less than the other part, namely, chemically heterogeneous and physically flat part), was analyzed using numerical simulations employing the front-tracking method and the generalized Navier boundary condition. We observed that the contact line was distorted with a logarithmic shape far from the defect; however, the distortion was dependent on the wall velocity. The apparent (averaged) dynamic contact angle of the wall with a defect was evaluated using a macroscopic energy balance. The apparent dynamic contact angles estimated from the energy balance agree well with the arithmetic averaged angles obtained from the present simulations. The macroscopic energy balance is useful to consider the effect of heterogeneity or roughness of the wall on the relation between the dynamic contact angle and contact line speed. Published by AIP Publishing. [<http://dx.doi.org/10.1063/1.4961490>]

## NOMENCLATURE

$A$	Area swept by contact line
$a$	Area of defect
$a_{\text{dry}}$	Dry area of defect after contact line's sweep
$Ca$	Capillary number, $\mu_l  \mathbf{u}_{\text{cl}}  / \sigma$
$D$	Diameter of defect
$D_{2D}, D_{3D}$	Two-dimensional and three-dimensional delta function
$d$	One-dimensional delta function
$d_1$	Supplementary function for defining $d$
$d\mathbf{n}$	Infinitesimal vector parallel to the wall across the diffused interface
$E_{\text{dry}}^*$	Nondimensional work to dry defect, $a_{\text{dry}} \cos \theta_{SD} / A$
$E_{\text{surf}}, E_{\text{surf}}^*$	Dimensional and nondimensional work done by surface deformation, $E_{\text{surf}}^* = E_{\text{surf}} / (A\sigma)$
$E_{\text{visc}}, E_{\text{visc}}^*$	Dimensional and nondimensional viscous dissipation, $E_{\text{visc}}^* = E_{\text{visc}} / (A\sigma)$
$F$	Body force due to the interfacial tension effect
$F_m$	Force normal to the interface at side m
$f_{\text{cl}}^e$	Wall tangent component of the force acting contact line
$f_m^e$	Force pulling the adjacent interface element at side m of element e
$g$	Gravitational acceleration
$k$	Unit vector in vertical upward direction
$L_{\text{cut}}$	Cutoff length for distorted contact line model

<sup>a)</sup>Author to whom correspondence should be addressed. Electronic mail: [yamayasu@kansai-u.ac.jp](mailto:yamayasu@kansai-u.ac.jp)

$L_x, L_y, L_z$	Region size in spanwise, wall-normal, and vertical direction
$l_{\text{cap}}$	Capillary length, $(\sigma/(\rho_1 g))^{1/2}$
$l_m^e$	Length of side $m$ of triangle element $e$
$l_{\text{micro}}$	Microscopic length scale parameter
$\mathbf{n}^e$	Unit normal of element $e$
$p$	Pressure
$R_0$	Length determined from tensional force by defect
$r$	Dimensionless distance
$T$	Period for the contact line to travel over the area $A$ , $(A/(UL_x))$
$T_d$	Time when the deformation of the contact line becomes maximum
$\mathbf{t}_m^e$	Unit tangent of side $m$ of triangle element $e$
$\mathbf{t}_w^e$	Unit normal of the contact line tangent to the wall
$U$	Moving wall speed
$\mathbf{u}$	Fluid velocity
$ \mathbf{u}_{\text{cl}} $	Contact line speed, $ \mathbf{u}_{\text{slip}}(\mathbf{x}_{\text{cl}}) $
$\mathbf{u}_{\text{slip}}$	Slip velocity on the wall, $\mathbf{u}(y = 0) - U\mathbf{k}$
$W$	Work done by the surface tension acting on the wall
$\mathbf{x}_{ijk}$	Position of fixed grid point $(x_i, y_j, z_k)$
$\mathbf{x}^*$	Irregular position respect to uniform grid
$z_0$	Undistorted level of the contact line, $z(x = 0)$
$\beta$	Slip coefficient
$\chi$	Nondimensional slip parameter, $\bar{\mu}/(\beta\Delta)$
$\Delta$	Uniform grid interval
$\Delta S_{\text{surf}}$	Increase of liquid surface
$\mu, \mu_g, \mu_l$	Viscosity of multi-fluid, gas, and liquid
$\bar{\mu}$	Arithmetic average viscosity
$\theta_s$	Static contact angle
$\theta_{s0}$	Static contact angle of wall except for defect
$\theta_{sD}$	Static contact angle of defect
$\theta_d$	Dynamic contact angle
$\theta_{dA}$	Apparent (averaged) contact angle
$\theta_{d\text{mean}}$	Arithmetic averaged contact angle
$\theta_{dyz}$	Dynamic contact angle in vertical plane
$\rho, \rho_g, \rho_l$	Density of multi-fluid, gas, and liquid
$\sigma, \sigma_{sg}, \sigma_{sl}$	Interfacial tension between liquid-gas, solid-gas, and solid-liquid
$\tau_{\text{wall}}^{\text{visc}}$	Viscous shear stress on the wall
$\tilde{\tau}^{\text{Young}}$	Unbalanced Young's stress

## I. INTRODUCTION

The wetting of a solid surface by a liquid is not only a physically interesting phenomenon but also a critical one in many industrial processes. The wettability is described by the contact angle, which is the angle between the solid-liquid and liquid-gas interfaces at the contact line; however, it is well known that the contact angle is dependent on the velocity of the contact line and shows hysteresis between advancing and receding. Since the tangential resultant of surface tension acting on droplet or bubble on solid wall may be controlled by the contact angle, the velocity dependence and the hysteresis of the contact angle have important effects on the performance of various engineering devices treating small amount of liquid, e.g., microfluidic actuation of droplets<sup>1</sup> or control of liquid column in a capillary.<sup>2,3</sup> The contact angle hysteresis might be considered due to chemical heterogeneity or physical roughness; however its detailed mechanism has never been fully described.

Many studies about contact angle hysteresis are summarized in some reviews.<sup>4-6</sup> To study the effect of chemical heterogeneity or physical roughness in detail, the contact line pinning and depinning at defects on the wall are treated. Joanny and de Gennes<sup>7</sup> and de Gennes<sup>8</sup> proposed a model

based on elasticity for the pinning at a single defect. Then, Nadkarni and Garoff<sup>9</sup> confirmed the logarithmic shape proposed by Joanny and de Gennes by experimental observation. Finally, Marsh and Cazabat<sup>10</sup> also observed the depinning from the single defect by experimental observation and confirmed the logarithmic shape. However, Marsh and Cazabat indicated that the characteristic velocity does not agree with the theory using a static contact angle based on the model by de Gennes<sup>8</sup> and considering that the dynamic contact angle is important. Moulinet *et al.*<sup>11</sup> observed the contact line passing a single defect and compared its relaxation behavior with that in the theoretical model by Ertas and Kardar;<sup>12</sup> these authors demonstrated that the fitted parameter of the model is roughly  $10^3$  times smaller than the theoretical expectation. Furthermore, theoretical approaches<sup>13–16</sup> and experimental approaches<sup>17–19</sup> have been performed; however, the dynamics of the moving contact line passing defects have never been fully described. Cubaud and Fermigier<sup>20</sup> studied the relation between the fraction of defects and apparent contact angle by experimental observation. Katoh *et al.*<sup>2</sup> proposed a model for the relation between the dynamic contact angle and contact line velocity by considering trapping of the contact line with defects and confirmed that the model can represent the experimentally observed relations.<sup>21</sup>

To date, there have not been many approaches using direct numerical simulation of the Navier–Stokes equation to study the wall defect because of the difficulty of the moving contact line representation. Wang *et al.*<sup>22</sup> performed Navier–Stokes simulations considering a nonuniform wall using a diffused interface method with the generalized Navier boundary condition (GNBC) proposed by Qian *et al.*<sup>23</sup> Ren and E<sup>24</sup> also performed this type of simulations using the level-set method with a slip model similar to GNBC. However, the defects treated in both simulations were one-dimensional periodic variations of wettability; thus, the contact line will never be deformed by the defects. Our group<sup>3,25</sup> proposed a simulation method using GNBC combined in a framework of the front-tracking method<sup>26</sup> and confirmed that the model can reasonably represent the moving contact line. In experiments, it is nearly impossible to perfectly prepare a homogeneous and smooth wall; however, in numerical simulations, a perfectly homogeneous and smooth wall with no hysteresis can be set easily. In our simulation model,<sup>3</sup> we can easily set a defect, which is a part that has different wettability. In this study, we perform numerical simulations of a moving contact line on a flat plate with a single defect (whose static contact angle is less than the other part, namely, chemically heterogeneous and physically flat part) and compare the results of the contact line profile with theoretical ones for quasi-static case<sup>9,27</sup> for validation. Then, we discuss the velocity dependency of the apparent contact angle and compare the average contact angle with the apparent contact angle estimated by a model considering macroscopic energy balance. The study was performed with the aim of understanding the dynamic contact angle on a heterogeneous or rough wall.

## II. NUMERICAL METHOD

### A. Front-tracking method

In the front-tracking method,<sup>26</sup> the gas–liquid interface is tracked by marker points, and the interface information is calculated by elements connecting markers. Using this information, the single-fluid equations are solved using the finite-difference method. The interval of advected marker points is not uniform; therefore, the interval should be adjusted by marker addition, deletion, or reconnection. To avoid this intricate process, we employed the level contour reconstruction method (LCRM),<sup>28</sup> which can treat the interface elements without logical connectivity. See Ref. 28 for the details of the LCRM and see Refs. 29 and 30 for the improvement of the volume conservation property of the LCRM. Furthermore in the present simulations, numerical instability caused by interface element reconstruction was alleviated by alternative use of two indicator functions defined at two-grid systems with half-grid-size gap.

The basic equations are the incompressible Navier–Stokes and continuity equations,

$$\rho \left[ \frac{\partial \mathbf{u}}{\partial t} + \nabla \cdot (\mathbf{u}\mathbf{u}) \right] = -\nabla p + \nabla \cdot [\mu(\nabla \mathbf{u} + \nabla \mathbf{u}^T)] + \mathbf{F} + \rho \mathbf{g}, \quad (1)$$

$$\nabla \cdot \mathbf{u} = 0, \quad (2)$$

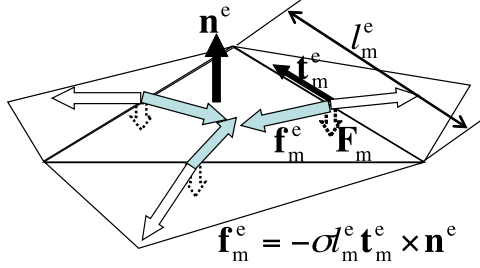


FIG. 1. Interfacial tension pulling the adjacent element.

where  $\mathbf{u}$  and  $p$  are the fluid velocity and pressure, respectively, and  $\mathbf{g}$  is the gravitational acceleration. The density  $\rho$  and viscosity  $\mu$  are given using an indicator function obtained from the unit normal of the interface elements. The body force  $\mathbf{F}$  is obtained from the interfacial tension effect, as shown later.

The flow field is determined by solving Equations (1) and (2) on fixed grid points and with the assistance of the markers' information for  $\rho$ ,  $\mu$ , and  $\mathbf{F}$ . Equations (1) and (2) are discretized in space by a second-order central finite-difference method on a staggered-grid system. A second-order Adams–Bashforth method is applied to advance the advection term in time, and a second-order Crank–Nicolson scheme is applied for the viscous term. The pressure is linked to Equation (2) by the simplified marker and cell algorithm, and the Poisson equation for pressure correction is solved using a multigrid method.

## B. Evaluation of interfacial tension effect and distribution to grid points

The gas-liquid interface is represented by a triangle element pulling its adjacent elements, as shown in Fig. 1. The force  $\mathbf{f}_m^e$  pulling the adjacent element at the common side (whose length is  $l_m^e$ ) is represented by the unit normal of the element  $\mathbf{n}^e$ , the unit tangent of the side  $\mathbf{t}_m^e$ , and the surface tension  $\sigma$  as follows:

$$\mathbf{f}_m^e = -\sigma l_m^e \mathbf{t}_m^e \times \mathbf{n}^e. \quad (3)$$

Obtaining the force pulling the common side for the adjacent element and distributing these forces onto grid points, the force normal to the interface  $\mathbf{F}_m$  corresponding to Laplace pressure jump (the resultant of  $\mathbf{f}_m^e$ , indicated by blue and white arrows shown in Fig. 1) can be represented. The force  $\mathbf{F}$  in Eq. (1) is obtained by distributing the force (3) onto the grid points using the weight function

$$\mathbf{F}(\mathbf{x}_{ijk}) = \sum_e \sum_m D_{3D}(\mathbf{x}_{ijk} - \mathbf{x}_m^e) \mathbf{f}_m^e, \quad (4)$$

where  $e$  represents the element,  $m$  represents a side of the element  $e$ , and  $\mathbf{x}_{ijk}$  is the position of a fixed grid point.

As suggested by Peskin,<sup>31</sup> we use the following function to approximate the delta function  $D_{3D}$ :

$$D_{3D}(\mathbf{x}_{ijk} - \mathbf{x}^*) = \frac{1}{\Delta^3} d\left(\frac{x_i - x^*}{\Delta}\right) d\left(\frac{y_j - y^*}{\Delta}\right) d\left(\frac{z_k - z^*}{\Delta}\right), \quad (5)$$

where  $\Delta$  is the uniform grid interval,  $\mathbf{x}^*$  is an interface position (whose relative position is irregular with respect to the uniform grid), and  $d$  is a one-dimensional function of the dimensionless distance  $r$ ,

$$d(r) = \begin{cases} d_1(r), & |r| \leq 1 \\ \frac{1}{2} - d_1(2 - |r|), & 1 < |r| < 2 \\ 0, & |r| \geq 2 \end{cases}, \quad (6)$$

where

$$d_1(r) = \frac{3 - 2|r| + \sqrt{1 + 4|r| - 4r^2}}{8}. \quad (7)$$

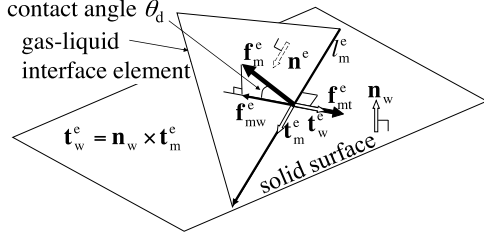


FIG. 2. Relation between interfacial tensions acting on the element adjacent to the solid surface.

The function (6) has the following features for discrete points  $x_i$  and any real  $x^*$ : (i) the summation  $\sum_i d((x_i - x^*)/\Delta)$  is strictly unity and (ii) the first moment  $\sum_i (x_i - x^*)d((x_i - x^*)/\Delta)$  is strictly zero. Therefore, the weight is always normalized, and the weight center position of the distribution is correctly represented only by discrete points.

### C. Boundary condition for moving contact line

In the process of evaluation of Eq. (3), if the side of the element is the contact line, as shown in Fig. 2, then the solid surface tension  $\sigma_{sg}$  and solid–liquid interfacial tension  $\sigma_{sl}$  are considered. The wall normal component of  $f_m^e$  is supposed to be supported by the reaction force of the rigid wall. The wall tangent component of the force acting contact line  $f_{cl}^e$  is represented by the unit normal of the contact line tangent to the wall  $t_w^e$  as

$$f_{cl}^e = f_{mt}^e + f_{mw}^e = (l_m^e \sigma_{sg} - l_m^e \sigma_{sl} + f_m^e \cdot t_w^e) t_w^e. \quad (8)$$

Using Young's equation with static contact angle  $\theta_s$  and dynamic contact angle  $\theta_d$ , Eq. (8) is represented as follows:

$$f_{cl}^e = l_m^e \sigma (\cos \theta_s - \cos \theta_d) t_w^e. \quad (9)$$

This unbalance force of Young's equation is used for GNBC as shown later and is not distributed to the grid points for  $\mathbf{F}$  (namely, not contained in Eq. (4)).

GNBC was proposed by Qian *et al.*<sup>23</sup> on the basis of MD simulations. One piece of evidence is that the tangential interaction force between the fluid molecules in a very thin layer adjacent to a wall and the wall molecules is proportional to the slip velocity. Another piece of evidence is that the interaction force acting on the very thin layer adjacent to the wall can be represented by the viscous shear stress on the wall  $\tau_{wall}^{visc}$  and unbalanced Young's stress  $\tilde{\tau}^{Young}$ . GNBC can then be represented as

$$\beta \mathbf{u}_{\text{slip}} = \tau_{wall}^{visc} + \tilde{\tau}^{Young}, \quad (10)$$

where  $\mathbf{u}_{\text{slip}}$  is the slip velocity on the wall and  $\beta$  is the slip coefficient. The unbalanced Young's stress is given by the integral,

$$\int_{\text{int}} \tilde{\tau}^{Young} \cdot d\mathbf{n} = \sigma (\cos \theta_s - \cos \theta_d), \quad (11)$$

where the integration is applied across the diffused interface along the direction parallel to the wall ( $d\mathbf{n}$  means the infinitesimal vector in that direction). Yamamoto *et al.*<sup>3</sup> proposed a numerical implementation of the stress using an approximation of the delta function used in the front-tracking method for the two-dimensional case. Then, in this three-dimensional case, we extend it straightforwardly as

$$\tilde{\tau}^{Young}(x_i, z_k) = \sum_{cl} D_{2D}(x_i - x_{cl}, z_k - z_{cl}) f_{cl}^e, \quad (12)$$

where  $cl$  represents the contact line and  $D_{2D}$  is the two-dimensional weight function considering only the  $x$  and  $z$  directions in Eq. (5). Then,  $\mathbf{u}_{\text{slip}}$  is obtained from Eq. (10) with Eqs. (12) and (9) and used as the boundary conditions on the wall.

Using GNBC as discussed in the work of Yamamoto *et al.*,<sup>3</sup> the divergence of the viscous stress is avoided because the large slip velocity occurs at the contact line. Moreover, because of the decrease in the viscous stress due to the large slip, the first term of the right-hand side of Eq. (10) is negligible compared with the second term. By the simplification, the nondimensional contact line velocity (i.e., the capillary number  $Ca \equiv \mu_l |\mathbf{u}_{cl}|/\sigma$ , where  $\mu_l$  is the viscosity of the liquid phase and  $|\mathbf{u}_{cl}|$  is the contact line speed corresponding to  $|\mathbf{u}_{slip}(\mathbf{x}_{cl})|$ ) is derived using Eqs. (10), (12), and (6) with  $\mathbf{x} = \mathbf{x}_{cl}$  and neglecting  $\tau_{wall}^{visc}$ .

$$Ca = \chi(\cos \theta_s - \cos \theta_d), \quad (13)$$

where  $\chi (= \bar{\mu}/(\beta\Delta))$  is the nondimensional slip parameter that represents the dynamic property of wetting.  $\bar{\mu}$  is the arithmetic average viscosity, and this treatment of viscosity weighting is discussed in the electronic Annex 1 in the online version of Yamamoto *et al.*<sup>3</sup> Since we use resolution-dependent distributions of the interfacial information in the front-tracking procedure, Eq. (12) depends on the grid resolution  $\Delta$ . Thus, the slip coefficient  $\beta$  cannot be treated as a physical parameter in the present procedure, and parameter  $\chi$  should be treated as the nondimensional slip parameter, as confirmed by Yamamoto *et al.*<sup>3</sup> Equation (13) represents the slip related to the deviation of the instantaneous contact angle from the static contact angle, and the contact line moves as making the contact angle to approach the static contact angle. The parameter  $\chi$  characterizes the response time of the contact line movement. A large value of  $\chi$  results in large  $Ca$ , and then, the contact angle rapidly approaches the static angle. The derivation of  $\chi$  is based on numerical procedure; however, this parameter based on the relation (13) represents the physical property as discussed above. In this GNBC-front-tracking model,  $\theta_s$  and  $\chi$  are the input parameters.

As demonstrated in the work of Yamamoto *et al.*,<sup>25</sup> the GNBC-front-tracking method exhibits grid resolution dependency without convergence for large capillary number case. The grid resolution dependency problems for moving contact line are also described for the other method<sup>32–35</sup> based on a matched asymptotic expansion.<sup>36</sup> To avoid the grid resolution dependency, Yamamoto *et al.*<sup>25</sup> proposed a method employing Cox's microscopic-macroscopic relation<sup>37</sup> using a microscopic length scale parameter  $l_{micro}$  with the GNBC. In the present study of numerical experiments, we simply set  $l_{micro}$  needed for our model to the grid size as a practical example, because we do not suppose any actual material as the wall (actually,  $l_{micro}$  is considered to be nanometric scale<sup>36</sup>). In the case of using grid size as  $l_{micro}$ , the grid scale contact angle can be associated directly with the microscopic one in the method using Cox's relation, and such cases are possible for  $Ca = O(10^{-3})$  as discussed in the work of Yamamoto *et al.*<sup>3</sup> In this study, the resolution is set to resolve a defect and the capillary number  $Ca$  is in  $O(10^{-3})$ ; thus, we suppose the grid size as the microscopic scale and avoid the resolution dependency effect by using the fixed grid size.

### III. TARGET AND CONDITION

Figure 3 shows the configuration of the present simulations. We treat a vertically withdrawing plate from a liquid bath with constant velocity. The lower part of the domain was filled with water ( $\rho_l = 998.2 \text{ kg/m}^3$ ,  $\mu_l = 1.002 \times 10^{-3} \text{ Pa s}$ ), and the upper part was filled with air ( $\rho_g = 1.205 \text{ kg/m}^3$ ,  $\mu_g = 1.822 \times 10^{-5} \text{ Pa s}$ ). Then, the surface tension is  $\sigma = 72.75 \times 10^{-3} \text{ N/m}$ . The plate, a moving wall with a constant velocity  $U$ , is generally smooth and homogeneous but has a single defect, which is more wettable than the other part. The defect is circular, and its diameter  $D$  is set to  $100 \mu\text{m}$ . The grid spacing  $\Delta$  is set to  $10 \mu\text{m}$ ; thus, the defect is resolved roughly by the grid system. The number of grid points is 80, 160, and 240 in the  $x$ ,  $y$ , and  $z$  directions, respectively. The uniform cubic grid is used for almost all cases; however, in the larger wall velocity cases in this study, the geometrically elongated grid in the  $z$  direction far away from the interface is used to relax the domain size effect ( $L_z = 2945 \mu\text{m}$  for  $0.2 \text{ m/s}$  wall velocity and  $L_z = 3597 \mu\text{m}$  for  $0.25 \text{ m/s}$ ). In the  $x$  direction, the periodic boundary condition is applied. The width  $L_x (= 800 \mu\text{m})$  is approximately  $0.3l_{cap}$ , where  $l_{cap} = (\sigma/(\rho_l g))^{1/2}$  is the capillary length. Therefore, we mention a single defect; however, the system practically corresponds to containing horizontally arrayed defects with period  $L_x$ . The boundary conditions are GNBC at  $y = 0$ , and gradient-free boundary condition at  $y = L_y$  and at both  $z$  ends. The still-water level is adjusted for each case for the liquid surface  $H$ .

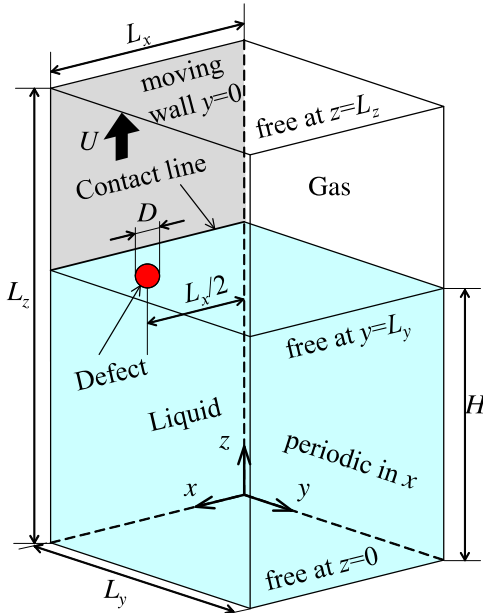


FIG. 3. Configuration of the present simulations.

to exist in the middle of the computational domain by controlling the base height of hydrostatic pressure.

The static contact angle of the wall  $\theta_{s0}$  except for the defect is maintained at  $90^\circ$  for all cases. The static contact angle of the defect  $\theta_{sD}$  is set from  $15^\circ$  to  $60^\circ$  with a  $15^\circ$  interval. The velocity of the wall  $U$  is set from  $0.05$  m/s to  $0.25$  m/s with a  $0.05$  m/s interval, with the capillary number corresponding to  $0.0007$ – $0.0034$ . The time step  $\Delta t$  is set to  $2.0 \times 10^{-6}$  s. The nondimensional slip parameter  $\chi$  for GNBC is set to  $0.02$ , close to a practical value to fit some experimental data.<sup>3</sup> Before performing simulations with defects, a fully developed steady state is achieved for each  $U$  using adequate step computations.

The grid size used in this study was decided by considering that the defect can be resolved enough (circular defect can be reproduced as shown in Fig. 5). The time increment was decided by considering Courant-Friedrichs-Lowy number criterion and the effect of acceleration by the surface force on the grid scale  $\Delta t(F/(\rho\Delta))^{1/2} < 0.4$  as confirmed in the electronic Annex 1 in the online version of Yamamoto *et al.*<sup>3</sup> As also confirmed in the reference, simulation results by our moving contact line model in two-dimensional front-tracking method are quite independent on time step size. In the present study, although the spatial and temporal resolution effects are not shown, we propose energy balance model as will be described later and evaluate the model with numerical results obtained by the fixed-resolution simulations. Even if the present numerical simulation cannot predict the specific real phenomena quantitatively, the qualitative tendency of the wetting dynamics can be evaluated.

## IV. RESULTS AND DISCUSSION

### A. Contact line behavior upon passing a defect

Figures 4 and 5 present snapshots of the liquid surface upon passing a defect with  $\theta_{sD} = 60^\circ$  and  $15^\circ$ , respectively, for  $U = 0.15$  m/s cases as samples. The time is adjusted to be zero, at which point the contact line just attaches to the defect. The region between the vertical white solid lines is the moving wall, the red bold circle on the wall is the defect, and the white dots are water surface markers used in the front-tracking. The defect moves upward with time and passes the contact line region. When the contact line passes over the defect, the contact line is trapped with the defect

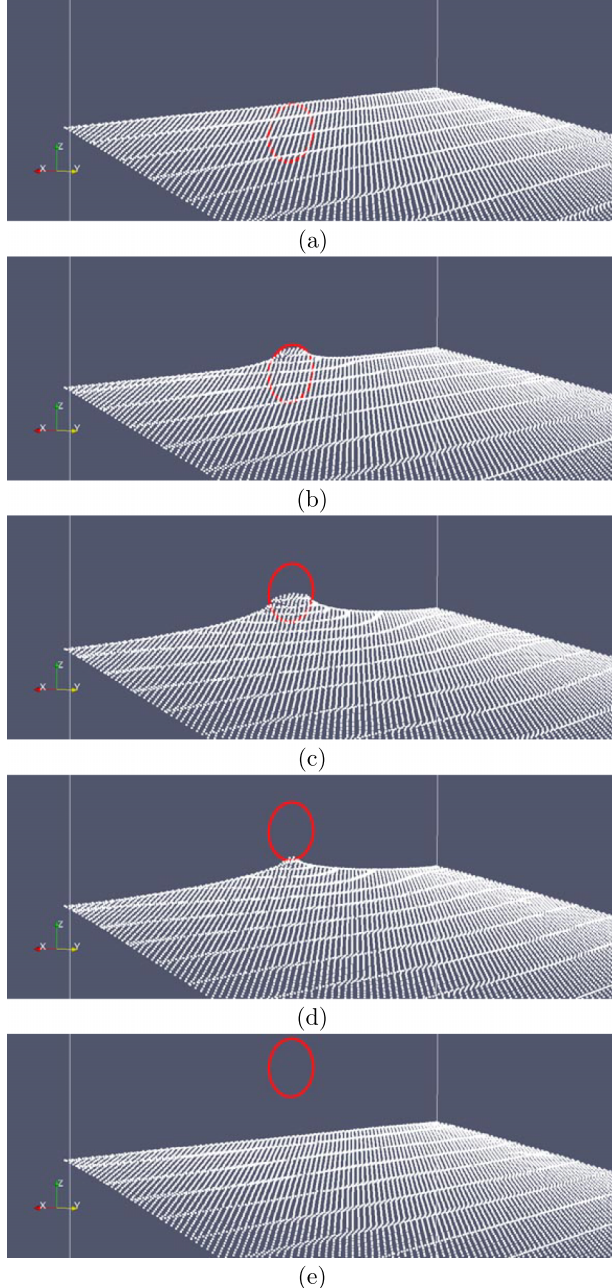


FIG. 4. Snapshots of the water surface for  $U = 0.15$  m/s,  $\theta_{\text{SD}} = 60^\circ$ , the white dots represent the interface markers, and the red bold circle represents the defect on the wall. (a) Time =  $-0.004$  ms. (b) Time =  $0.236$  ms. (c) Time =  $0.676$  ms. (d) Time =  $0.916$  ms. (e) Time =  $1.176$  ms.

because of better wettability, and the contact line is distorted by the trapping. Thereafter, the contact line is released from the defect and slips to the straight shape, the same as that before the trapping. Furthermore, for strong wettability of the defect ( $\theta_{\text{SD}} = 15^\circ$ ) shown in Fig. 5, the strong trapping of the contact line leaves a water drop on the defect. The more detailed investigation is needed to predict whether leaving a droplet or not, and it is left for future work. Similar contact line deformations are observed in other cases (the results are not shown here).

The maximum distorted profiles of the contact line for  $\theta_{\text{SD}} = 45^\circ$  and  $60^\circ$  are shown in Fig. 6. The maximum distortion is determined from the maximum area of the liquid surface. For example, the maximum distortion for the  $U = 0.15$  m/s and  $\theta_{\text{SD}} = 60^\circ$  condition is observed at the moment

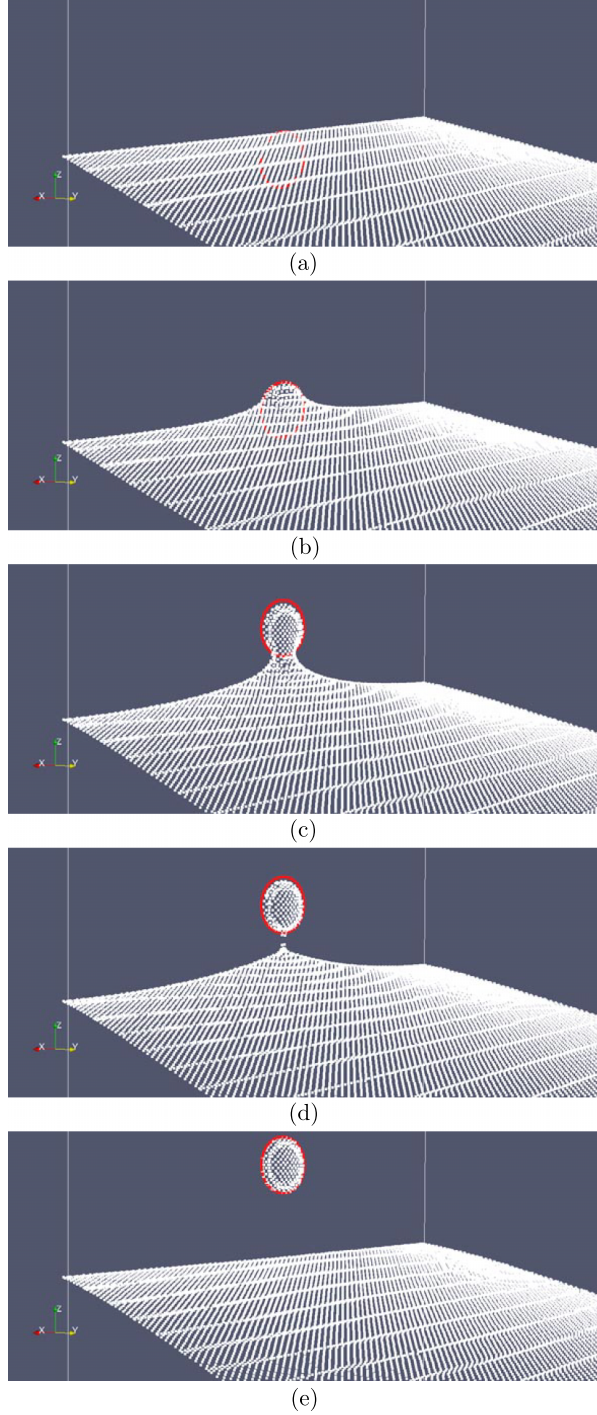


FIG. 5. Snapshots of the water surface for  $U = 0.15$  m/s,  $\theta_{SD} = 15^\circ$ ; see caption of Fig. 4. (a) Time =  $-0.004$  ms. (b) Time =  $0.416$  ms. (c) Time =  $1.176$  ms. (d) Time =  $1.276$  ms. (e) Time =  $1.556$  ms.

shown in Fig. 4(c). The black bold solid lines are theoretical profiles for quasi-static case<sup>9,27</sup> using

$$z(x) - z_0 = R_0 \ln \frac{L_{\text{cut}}}{|x - L_x/2|} \quad \text{for} \quad \left| x - \frac{L_x}{2} \right| > \frac{D}{2}, \quad (14)$$

where  $z_0$  is the undistorted level of the contact line (we use  $z(x = 0)$  for our simulated results),  $R_0$  is the length determined from tensional force ( $R_0$  corresponds to the radius of cross section of

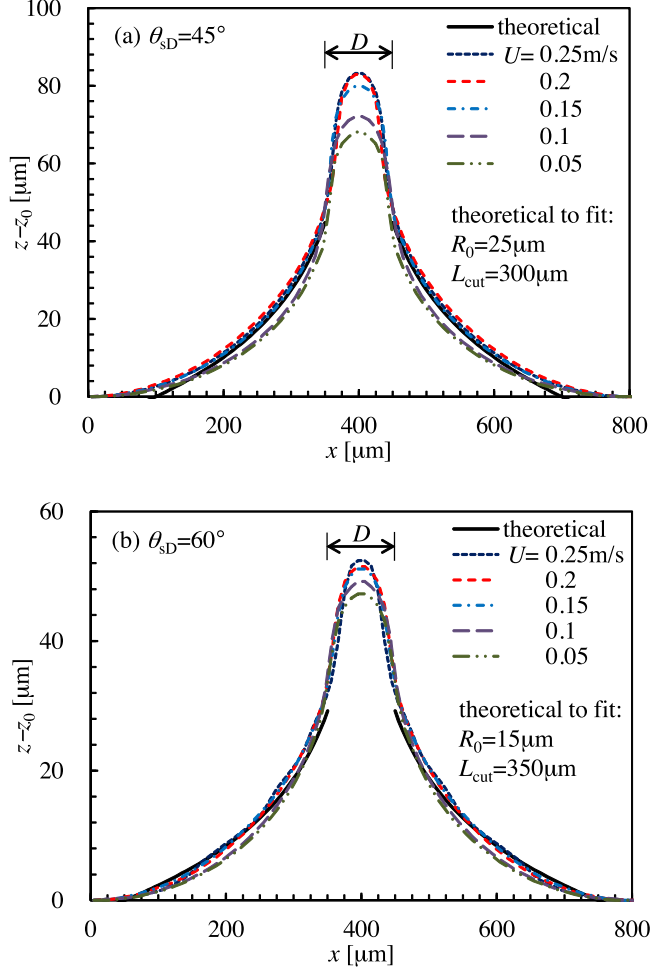


FIG. 6. Contact line profiles at maximum deformation: (a)  $\theta_{\text{SD}} = 45^\circ$ , (b)  $\theta_{\text{SD}} = 60^\circ$ .  $U = 0.05, 0.1, 0.15, 0.2$ , and  $0.25 \text{ m/s}$  correspond to  $Ca = 0.0007, 0.0014, 0.0021, 0.0028$ , and  $0.0034$ , respectively. Theoretical curves (for quasi-static case) are obtained by Eq. (14).

stretched region with assumption of circular cross section), and  $L_{\text{cut}}$  is the cutoff length representing the distorted region.  $R_0$  and  $L_{\text{cut}}$  are adjusted to fit the simulated results for each  $\theta_{\text{SD}}$  case, and the fitted values are shown in the figures. Because Eq. (14) is a very simple model representing interface shape near the defect considering stretching force, we cannot give a strict value for  $R_0$ . The important result of this simple theoretical model is logarithmic profile of contact line, so we confirm that the present simulations can reproduce such a logarithmic profile. As mentioned above,  $R_0$  should be in order of radius of the defect, and our results actually show such magnitude. Because  $L_{\text{cut}}$  does not have to coincide to the periodic length strictly in this simple model, we just paid attention of its order of magnitude, so we treated both  $R_0$  and  $L_{\text{cut}}$  as fitting parameters.  $L_{\text{cut}}$  is almost near the half-size of the periodic region (which is much less than the capillary length). A more wettable defect ( $\theta_{\text{SD}} = 45^\circ$ ) pulls more strongly; thus,  $R_0$  is larger for  $\theta_{\text{SD}} = 45^\circ$  than for  $\theta_{\text{SD}} = 60^\circ$ . For these cases (the contact line movement is very slow and may be considered as quasi-static), the contact line pinning a single defect is characterized by logarithmic profiles, as theoretically estimated by Joanny and de Gennes<sup>7</sup> and experimentally confirmed by Nadkarni and Garoff.<sup>9</sup> Therefore, we consider this finding as the evidence of the reliability of the present simulation.

The contact line distortion appears to be almost independent of the wall velocity  $U$  except in the defect ( $|x - L_x/2| < D/2$ ) in Fig. 6; however, the pinning top is roughly near the center of the defect for all cases, and the profiles relative to the pinning top depend on the wall velocity. The contact line slips with speed of  $-U$  at steady state without the defect. For the part far away from the

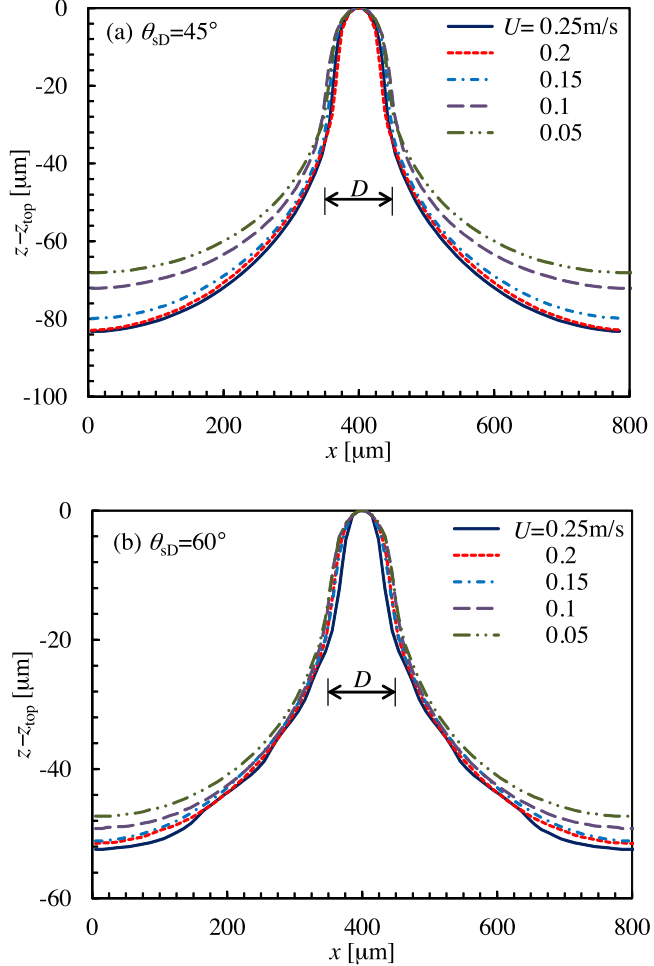


FIG. 7. Contact line profiles relative to the pinning top at maximum deformation: (a)  $\theta_{\text{SD}} = 45^\circ$ , (b)  $\theta_{\text{SD}} = 60^\circ$ .

defect, the effect of defect becomes weaker on the contact line shape, so the velocity dependency cannot be found for the part far away from the defect as in Fig. 6. However just near the defect, the contact line is deformed by the pinning at the defect, and the deformation depends on the wall speed. Fig. 7 presents the profiles relative to the pinning top, and we consider that these velocity dependent profiles might be more important for the dynamic contact angle. From Fig. 7, we can see that the contact line distortion depends on the wall velocity and that a larger wall velocity causes a larger distortion of the contact line. This velocity-dependent profile may affect the dynamic contact angle as will be discussed later.

## B. Contact angle dynamics upon passing a defect

Figure 8 shows the dynamic contact angle  $\theta_d$  and the contact line's vertical velocity relative to the wall  $u_{\text{slip}z}$  at  $x = L_x/2$  (the defect center is on  $x = L_x/2$  and the angle at  $x = L_x/2$  is easily observed because the contact line is locally horizontal) for several  $\theta_{\text{SD}}$  and  $U$  cases.

From  $t = 0$  s (corresponding to the instance that the contact line just attaches to the defect) in all cases, the dynamic contact angles'  $\theta_d$  values decrease from the steady-state values slightly smaller than  $\theta_{s0} = 90^\circ$  ( $\theta_d = \cos^{-1}(\cos \theta_{s0} + \mu U / (\chi \sigma))$  from Eq. (13)) and the slip velocities  $u_{\text{slip}z}$  change to zero from the wall velocities  $-U$ . The contact lines are trapped and the contact angles gradually decrease to the minimum. The weak wettability defect (larger  $\theta_{\text{SD}}$ ) cannot hold the slip; thus, the absolute value of the slip velocities roughly increases as  $\theta_{\text{SD}}$ . Then, suddenly, each contact angle starts to increase, and the corresponding slip velocity shows a negative spike corresponding

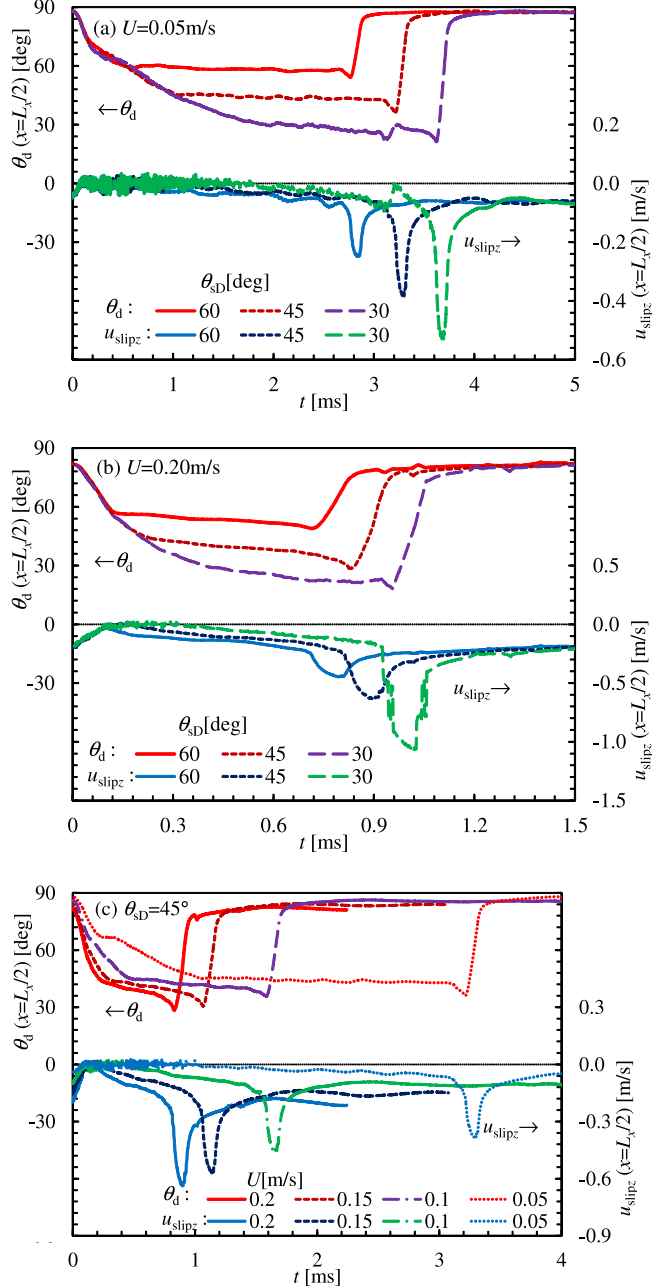


FIG. 8. Dynamic contact angle and contact line velocity passing through the center of the defect: (a)  $U = 0.05$  m/s, (b)  $U = 0.20$  m/s, and (c)  $\theta_{SD} = 45^\circ$ .

to fast slip motion. This moment is when the contact line passes the end of the defect and is just released from the trapping. After this moment, the contact angles return to the steady-state values, and the slip velocities approach the wall velocity  $-U$ . A more wettable defect (smaller  $\theta_{SD}$ ) traps the contact line longer because the local dynamic contact angle should decrease to approach the steady dynamic contact angle for the defect's static contact angle. There are undershoots of the contact angle that occurred before the contact line reaches the bottom of the defect. The reason is just the contact line likes to stay in more wettable part. The contact line clings to the defect, then the contact angle shows undershoot. When the clinging is off, the interface shape is going back to straight shape with large slip velocity. However the inertia is dissipated soon by large viscosity effect, so overshoot cannot be observed at the recovering time.

When the contact line reaching the defect, the contact angle of the centerline  $\theta_d(x = L_x/2)$  becomes larger than  $\theta_{sD}$ , so the slip velocity should be positive. However, the contact line around the centerline keeps its negative slip velocity, so the contact line of the center line cannot keep the positive slip velocity and show oscillation around zero before reaching  $\theta_{sD}$  as shown in Fig. 8. When  $\theta_d$  becomes smaller than  $\theta_{sD}$ , the contact line moves with negative slip velocity.  $\theta_d$  gets gradually smaller than  $\theta_{sD}$  after reaching  $\theta_{sD}$ , because the contact line is pulled by the upward moving wall. If the defect is long in the vertical direction,  $\theta_{sD}$  approaches to the steady dynamic angle of  $\cos^{-1}(\cos \theta_{sD} - \mu_l U / (\chi \sigma))$ . Fig. 8(c) shows that for a larger wall velocity, shorter times are needed to reach the minimum contact angle and the absolute value of the slip velocity peak by release from the defect is larger.

### C. Estimation of apparent dynamic contact angle

Here, we consider the energy balance during the contact line movement over the wall area  $A$  containing the defect of area  $a$ , as shown in Fig. 9. The wall surface  $A$  corresponds to the area swept by the contact line from the top of the defect to the position where it is recovered to an almost straight shape. Note that the ratio  $a/A$  is approximately 3%–6% in this study. While the contact line moves over the area  $A$ , the surface tension acting on the wall performs the work  $W$  written as

$$W = A\sigma \cos \theta_{dA}, \quad (15)$$

where  $\theta_{dA}$  represents the apparent (averaged) contact angle observed on the inhomogeneous wall. The work of Eq. (15) results from the sum of several kinds of works during the contact line movement. Thus, the energy balance equation can be written as

$$A\sigma \cos \theta_{dA} = a_{dry}\sigma \cos \theta_{sD} + (A - a)\sigma \cos \theta_{s0} + E_{surf} + E_{visc}. \quad (16)$$

In the right-hand side of the above equation, the first and second terms correspond to the work to dry the defect and the other wall surface excluding the defect, respectively. These values can be estimated from Young's equation.  $a_{dry}$  is the dry area of the defect after contact line's sweep. For the case with a drop remaining on the defect, as observed in Fig. 5,  $a_{dry}$  become smaller than  $a$  because the defect remains wetted. The third term  $E_{surf}$  in Eq. (16) is the surface energy increase (work to deform the liquid surface) and is estimated as

$$E_{surf} = \sigma \Delta S_{surf}, \quad (17)$$

where  $\Delta S_{surf}$  represents the increase of the liquid surface and is calculated from the sum of the element area in front-tracking as the difference between the maximum and steady states. For the case with a drop remaining on the defect, the liquid surface area on the drop is also considered for  $\Delta S_{surf}$  to calculate  $E_{surf}$ . The fourth term  $E_{visc}$  in the right-hand side of Eq. (16) is the viscous dissipation which can be calculated from the viscous stress on the wall  $\tau_{wall}^{visc}$  as

$$E_{visc} = \int_0^T \iint \tau_{wall}^{visc} U dx dz dt. \quad (18)$$

$T(\equiv A/(UL_x))$  is the period for the contact line to travel over the area  $A$ , as shown in Fig. 9. The total energy on the right-hand side of Eq. (16) should be supplied from the surface tension acting on

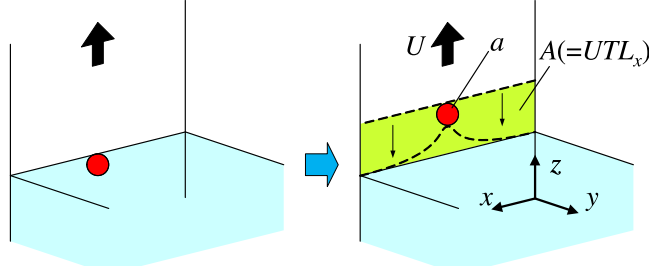


FIG. 9. Schematic of the contact line traveling over wall area  $A$  with defect of area  $a$ .

the wall, as represented by the left-hand side in which we define the apparent dynamic contact angle as  $\theta_{dA}$  on the wall. Because each term on the right-hand side can be obtained from the numerical results, we can estimate  $\theta_{dA}$  using Eq. (16). Note that if  $E_{surf}$  and  $E_{visc}$  are not counted, the energy balance equation (16) corresponds to the one for the quasi-static movement of contact line.<sup>38</sup>

It is noted that  $E_{visc}$  of Eq. (18) include the work  $E_{surf}$  of Eq. (17) in itself because the energy of surface deformation is released when the contact line separates from the defect and is dissipated until the contact line recovers its straight shape. So, the effect of  $E_{surf}$  should be eliminated from  $E_{visc}$  for Eq. (16). To eliminate the effect of  $E_{surf}$  on  $E_{visc}$ , here, the viscous dissipation was approximately estimated using the viscous stress on the wall until the contact line started to separate from the defect (i.e., the deformation of the contact line reached a maximum). The viscous dissipation  $E_{visc}$  was calculated using the following equation:

$$E_{visc} = \frac{T}{T_d} \int_0^{T_d} \iint \tau_{wall}^{visc} U dx dz dt, \quad (19)$$

where  $T_d$  represents the time when the deformation of the contact line becomes maximum and this modification means extrapolation of the value during  $T$  from the one during  $T_d$ .

Equation (16) proposed here means that the dynamic contact angle should be determined from each contribution of works appearing in the right-hand side. To verify the validity of the energy balance equation (16), the apparent dynamic contact angle is compared with the arithmetic averaged contact angle defined as

$$\theta_{dmean} = \cos^{-1} \left( \frac{1}{TL_x} \int_0^T \int_0^{L_x} \cos \theta_{dyz} dx dt \right), \quad (20)$$

where  $\theta_{dyz}$  represents the local dynamic contact angle in vertical plane actually observed on the wall. Then  $\theta_{dmean}$  was compared with  $\theta_{dA}$  in Eq. (16) determined from the sum of each work in the right-hand side estimated from the numerical results.

Figure 10 shows a sample of the horizontal distribution of  $\theta_{dyz}$  for  $\theta_{sD} = 45^\circ$  and  $U = 0.2$  m/s at the maximum deformation instant. For the part far away from the defect,  $\theta_{dyz} \sim \theta_d < \theta_{s0}$ , so the contact line slips downward. For the part  $x \sim L_x/2 \pm D/2$ , the interface is parallel to  $y - z$  plane, so  $\theta_{dyz}$  changes rapidly. For inside of the defect,  $\theta_{dyz} \sim \theta_d \lesssim \theta_{sD}$ , so the contact line is trapped (slightly slipping downward). For just outside the defect (the part where the contact line is vertically oriented as shown in Figs. 6 and 7), the interface is elongated in vertical (approaching parallel to the wall), so  $\theta_{dyz}$  becomes less than  $\theta_d$ .

Figure 11 shows the swept area  $A$  (a) and each term of Eq. (16) nondimensionalized by  $A\sigma$ , the first term (b),  $E_{surf}$  (c), and  $E_{visc}$  (d) as functions of the nondimensional wall velocity  $Ca = \mu_i U / \sigma$ . The second term of Eq. (16) is zero because  $\theta_{s0} = 90^\circ$  in this study.

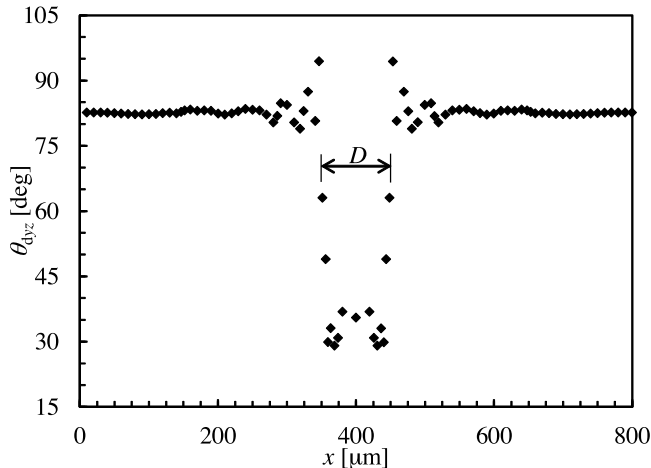


FIG. 10. Horizontal distribution of local dynamic contact angle in vertical plane  $\theta_{dyz}$ .

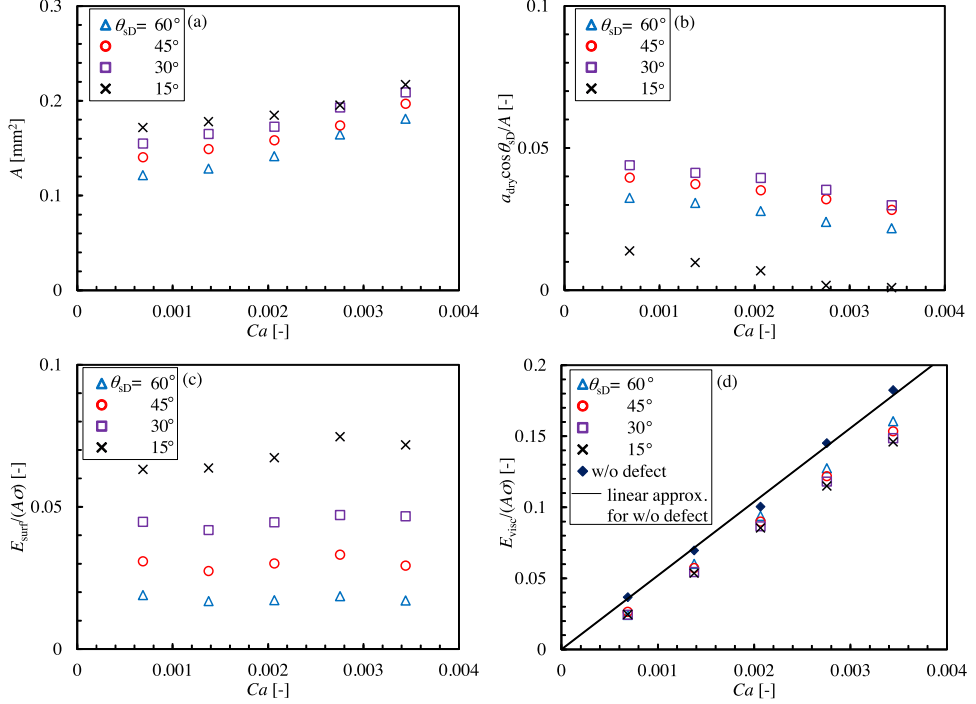


FIG. 11. Swept area  $A$  by contact line until being straight (a), work to dry the defect (b), work done by liquid surface deformation (c), and viscous dissipation (d). (b), (c), and (d) are nondimensionalized by  $A\sigma$ .

The swept area  $A$  increases with wall velocity  $Ca$  and also increases with decreasing  $\theta_{SD}$ , because larger  $Ca$  and smaller  $\theta_{SD}$  cause larger interface deformation and it takes longer time for the contact line to recover its straight shape.

The nondimensionalized work to dry the defect  $E_{dry}^*(\equiv a_{dry} \cos \theta_{SD} / A)$  decreases with  $Ca$  because  $A$  is larger for larger  $Ca$  and  $a_{dry} \approx a$  ( $a$  is constant) except for  $\theta_{SD} = 15^\circ$ . Except for  $\theta_{SD} = 15^\circ$ ,  $E_{dry}^*$  increases with  $\cos \theta_{SD}$ . For  $\theta_{SD} = 15^\circ$ ,  $E_{dry}^*$  approaches to zero with  $Ca$  increasing, because a drop remains on the defect and  $a_{dry}$  approaches to zero.

The nondimensional work done by surface deformation  $E_{surf}^*(\equiv E_{surf}/(A\sigma))$  increases with decreasing  $\theta_{SD}$  because smaller  $\theta_{SD}$  causes a larger surface deformation. The velocity dependences of  $E_{surf}^*$  are not obvious only by Fig. 11(c); however, almost flat profiles of the normalized value by  $A$  mean that larger  $Ca$  causes larger  $E_{surf}$  because  $A$  increases with  $Ca$  as shown in Fig. 11(a).

The nondimensional viscous dissipation  $E_{visc}^*(\equiv E_{visc}/(A\sigma))$  for the case without defects linearly increases with  $Ca$ . Without a defect ( $\Delta S_{surf} = 0$  and  $a = 0$ ), Eq. (16) reduces to  $E_{visc} = A\sigma(\cos \theta_{dA} - \cos \theta_{s0})$ . Furthermore, using Eq. (13), the relation  $E_{visc}^* = Ca/\chi$  is obtained. Thus, the linear relation between  $E_{visc}^*$  and  $Ca$  is reasonable for the case without defects.  $E_{visc}^*$  for the cases with defects slightly decreases from the case without defect because viscous dissipation is suppressed while contact line trapping (with no viscous friction by moving with the wall). And, the smaller  $\theta_{SD}$  decreases  $E_{visc}^*$  because of strong trapping. Furthermore, the large velocity dependences of  $E_{visc}^*$  are considered to affect the apparent contact angle's velocity dependence.

Figure 12 shows  $\theta_{dA}$  and  $\theta_{dmean}$  calculated from Eqs. (16) and (20), respectively, as functions of  $Ca$ .  $\theta_{dA}$  shows good agreement with  $\theta_{dmean}$  for each  $\theta_{SD}$  and  $Ca$ ; therefore, the estimation using Eq. (16) is valid. The apparent dynamic contact angle on the wall with a single defect can be represented by considering works performed by the defect; in particular, the liquid surface deformation affects the apparent contact angle's dependency on the wall velocity. We find that for  $\theta_{SD} \geq 30^\circ$  the smaller  $\theta_{SD}$  (more wettable defect) reduces the apparent dynamic contact angle  $\theta_d$ , and  $\theta_d$  of  $\theta_{SD} = 15^\circ$  is larger than that of  $\theta_{SD} = 30^\circ$ . The reverse of tendency is caused by a remaining drop on the defect for the case of  $\theta_{SD} = 15^\circ$ . The larger apparent contact angles of  $\theta_{SD} = 15^\circ$  than the case of  $\theta_{SD} = 30^\circ$  are observed because the decreasing effect of  $a_{dry}$  shown in Fig. 11(b) is larger than the

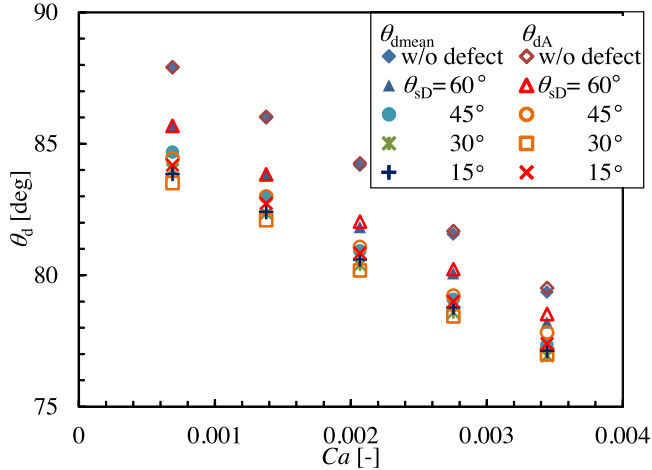


FIG. 12. Apparent dynamic contact angle  $\theta_{dA}$  estimated from macroscopic energy balance and arithmetic averaged dynamic contact angle  $\theta_{dmean}$ .

increasing effect of  $E_{surf}$  shown in Fig. 11(c). Thus for the extremely wettable defect, there are cases that the heavy work to dry such wettable defect is avoided, and in such cases, behavior of the most part of fluid except for remaining drop becomes equivalent for the case with less wettable defect (with large apparent contact angle).

The present simulation can reproduce such complex phenomena and the proposed macroscopic energy balance can predict the apparent contact angle even for such a complex case. So if liquid surface deformation and drop adhesion area are measured or modeled, the present energy Equation (16) may be very useful to estimate the average behavior of the contact line. More dense defects will be considered in future studies.

## V. CONCLUSION

We performed numerical simulations of the Navier–Stokes equation with a generalized Navier boundary condition for withdrawing a plate with a single wettable defect from a liquid bath. We observed that the contact line distorted with a logarithmic shape far from the defect; however, the distortion was dependent on the wall velocity. The apparent dynamic contact angle of the wall with a defect was evaluated using a macroscopic energy balance. The estimated apparent dynamic contact angles agree well with the arithmetic averaged angles obtained from the present simulations. Both the viscous dissipation and the work performed by the surface deformation increased with the wall speed because of the surface deformation. The macroscopic energy balance is useful to consider the effect of the wall heterogeneity or roughness on the relation between the dynamic contact angle and contact line speed.

## ACKNOWLEDGMENTS

This study was partially supported by JSPS KAKENHI Grant No. 25420135. The authors are grateful to Mr. Hajime Kusumoto for performing additional simulations.

- <sup>1</sup> A. A. Darhuber and S. M. Troian, “Principles of microfluidic actuation by modulation of surface stresses,” *Annu. Rev. Fluid Mech.* **37**, 425–455 (2005).
- <sup>2</sup> K. Katoh, T. Wakimoto, and S. Nitta, “A study on capillary flow under the effect of dynamic wetting,” *J. Jpn. Soc. Exp. Mech.* **10**(Special Issue), s62–s66 (2010).
- <sup>3</sup> Y. Yamamoto, T. Ito, T. Wakimoto, and K. Katoh, “Numerical simulations of spontaneous capillary rises with very low capillary numbers using a front-tracking method combined with generalized Navier boundary condition,” *Int. J. Multiphase Flow* **51**, 22–32 (2013).
- <sup>4</sup> P. G. de Gennes, “Wetting: Statics and dynamics,” *Rev. Mod. Phys.* **57**, 827–863 (1985).
- <sup>5</sup> L. Leger and J. F. Joanny, “Liquid spreading,” *Rep. Prog. Phys.* **55**, 431–486 (1992).

- <sup>6</sup> D. Bonn, J. Eggers, J. Indekeu, J. Meunier, and E. Rolley, “Wetting and spreading,” *Rev. Mod. Phys.* **81**, 739–805 (2009).
- <sup>7</sup> J. F. Joanny and P. G. de Gennes, “A model for contact angle hysteresis,” *J. Chem. Phys.* **81**, 552–562 (1984).
- <sup>8</sup> P. G. de Gennes, “Physique des surfaces et des interfaces — Dynamique d’une ligne triple,” *C. R. Acad. Sci. Paris, II* **302**, 731–733 (1986).
- <sup>9</sup> G. D. Nadkarni and S. Garoff, “An investigation of microscopic aspects of contact angle hysteresis: Pinning of the contact line on a single defect,” *Europhys. Lett.* **20**, 523–528 (1992).
- <sup>10</sup> J. A. Marsh and A. M. Cazabat, “Dynamics of contact line depinning from a single defect,” *Phys. Rev. Lett.* **71**, 2433–2436 (1993).
- <sup>11</sup> S. Moulinet, C. Guthmann, and E. Rolley, “Dissipation in the dynamics of a moving contact line: Effect of the substrate disorder,” *Eur. Phys. J. B* **37**, 127–136 (2004).
- <sup>12</sup> D. Ertas and M. Kardar, “Critical dynamics of contact line depinning,” *Phys. Rev. E* **49**, R2532–R2535 (1994).
- <sup>13</sup> E. Raphaël and P. G. de Gennes, “Dynamics of wetting with nonideal surfaces. The single defect problem,” *J. Chem. Phys.* **90**, 7577–7584 (1989).
- <sup>14</sup> J. F. Joanny and M. O. Robbins, “Motion of a contact line on a heterogeneous surface,” *J. Chem. Phys.* **92**, 3206–3212 (1990).
- <sup>15</sup> J. M. Schwarz and D. S. Fisher, “Depinning with dynamic stress overshoots: Mean field theory,” *Phys. Rev. Lett.* **87**, 096107-1–096107-4 (2001).
- <sup>16</sup> V. S. Nikolayev, S. L. Gavrilyuk, and H. Gouin, “Modeling of the moving deformed triple contact line: Influence of the fluid inertia,” *J. Colloid Interface Sci.* **302**, 605–612 (2006).
- <sup>17</sup> E. Schäffer and P. Wong, “Contact line dynamics near the pinning threshold: A capillary rise and fall experiment,” *Phys. Rev. E* **61**, 5257–5277 (2000).
- <sup>18</sup> J. Bico, C. Tordeux, and D. Quéré, “Rough wetting,” *Europhys. Lett.* **55**, 214–220 (2001).
- <sup>19</sup> S. M. M. Ramos, E. Charlaix, A. Benyagoub, and M. Toulemonde, “Wetting on nanorough surfaces,” *Phys. Rev. E* **67**, 031604-1–031604-6 (2003).
- <sup>20</sup> T. Cubaud and M. Fermigier, “Advancing contact lines on chemically patterned surfaces,” *J. Colloid Interface Sci.* **269**, 171–177 (2004).
- <sup>21</sup> K. Katoh, T. Wakimoto, Y. Yamamoto, and T. Ito, “Dynamic wetting behavior of a triple-phase contact line in several experimental systems,” *Exp. Therm. Fluid Sci.* **60**, 354–360 (2015).
- <sup>22</sup> X. P. Wang, T. Qian, and P. Sheng, “Moving contact line on chemically patterned surfaces,” *J. Fluid Mech.* **605**, 59–78 (2008).
- <sup>23</sup> T. Qian, X. P. Wang, and P. Sheng, “Molecular scale contact line hydrodynamics of immiscible flows,” *Phys. Rev. E* **68**, 016306-1–016306-15 (2003).
- <sup>24</sup> W. Ren and W. E, “Contact line dynamics on heterogeneous surfaces,” *Phys. Fluids* **23**, 072103-1–072103-9 (2011).
- <sup>25</sup> Y. Yamamoto, K. Tokieda, T. Wakimoto, T. Ito, and K. Katoh, “Modeling of the dynamic wetting behavior in a capillary tube considering the macroscopic–microscopic contact angle relation and generalized Navier boundary condition,” *Int. J. Multiphase Flow* **59**, 106–112 (2014).
- <sup>26</sup> S. O. Unverdi and G. Tryggvason, “A front-tracking method for viscous, incompressible, multi-fluid flows,” *J. Comput. Phys.* **100**, 25–37 (1992).
- <sup>27</sup> P. G. de Gennes, F. Brochard-Wyart, and D. Quéré, *Capillarity and Wetting Phenomena: Drops, Bubbles, Pearls, Waves* (Springer, 2003).
- <sup>28</sup> S. Shin and D. Juric, “Modeling three-dimensional multiphase flow using a level contour reconstruction method for front tracking without connectivity,” *J. Comput. Phys.* **180**, 427–470 (2002).
- <sup>29</sup> S. Shin and D. Juric, “High order level contour reconstruction method,” *J. Mech. Sci. Technol.* **21**, 311–326 (2007).
- <sup>30</sup> Y. Yamamoto and T. Uemura, “Numerical simulation of multiphase flows by level contour reconstruction method (improvement of volume conservation property),” *Trans. Jpn. Soc. Mech. Eng.* **77**, 237–246 (2011) (in Japanese).
- <sup>31</sup> C. S. Peskin, “The immersed boundary method,” *Acta Numer.* **11**, 479–517 (2002).
- <sup>32</sup> S. Afkhami, S. Zaleski, and M. Bussmann, “A mesh-dependent model for applying dynamic contact angles to VOF simulations,” *J. Comput. Phys.* **228**, 5370–5389 (2009).
- <sup>33</sup> J.-B. Dupont and D. Legendre, “Numerical simulation of static and sliding drop with contact angle hysteresis,” *J. Comput. Phys.* **229**, 2453–2478 (2010).
- <sup>34</sup> Y. Sui and P. D. M. Spelt, “An efficient computational model for macroscale simulations of moving contact lines,” *J. Comput. Phys.* **242**, 37–52 (2013).
- <sup>35</sup> Y. Sui, H. Ding, and P. D. M. Spelt, “Numerical simulations of flows with moving contact lines,” *Annu. Rev. Fluid Mech.* **46**, 97–119 (2014).
- <sup>36</sup> J. H. Snoeijer and B. Andreotti, “Moving contact lines: Scales, regimes, and dynamical transitions,” *Annu. Rev. Fluid Mech.* **45**, 269–292 (2013).
- <sup>37</sup> R. Cox, “The dynamics of the spreading of liquids on a solid surface. I. Viscous flow,” *J. Fluid Mech.* **168**, 169–194 (1986).
- <sup>38</sup> D. Li and A. W. Neumann, “Thermodynamic status of contact angles,” in *Applied Surface Thermodynamics*, edited by A. W. Neumann and J. K. Spelt (Marcel Dekker, 1996), pp. 109–168.